Study of collision and γ-cascade times following neutron-capture processes in cryogenic detectors

G. Soum-Sidikov,[1,*] H. Abele,[2] J. Burkhart,[3] F. Cappella,[4] N. Casali,[4] R. Cerulli,[5,6] A. Chalil,[1,7] A. Chebboubi,[7] J-P. Crocombette,[8] G. del Castello,[9,10] M. del Gallo Roccagiovine,[9,10] A. Doblhammer,[2] S. Dorer,[2] A. Erhart,[11] A. Giuliani,[12] C. Goupy,[1] F. Gunsing,[1] E. Jericha,[2] M. Kaznacheeva,[11] A. Kinast,[11] H. Kluck,[3] A. Langenkämper,[11] T. Lasserre,[1,11] A. Letourneau,[1] D. Lhuillier,[1] O. Litaize,[7] P. de Marcillac,[12] S. Marnieros,[12] R. Martin,[1] T. Materna,[1] E. Mazzucato,[1] C. Nones,[1] T. Ortmann,[11] L. Pattavina,[6,13] D. V. Poda,[12] L. Peters,[11] J. Rothe,[11] N. Schermer,[11] J. Schieck,[2,3] S. Schönert,[11] O. Serot,[7] L. Stodolsky,[14] R. Strauss,[11] L. Thulliez,[1] M. Vignati,[9,10] M. Vivier,[1] V. Wagner,[11] and A. Wex[11]

(CRAB Collaboration)

[1]*IRFU, CEA, Université Paris-Saclay, 91191 Gif-sur-Yvette, France*
[2]*TU Wien, Atominstitut, 1020 Wien, Austria*
[3]*Institut für Hochenergiephysik der Österreichischen Akademie der Wissenschaften, A-1050 Wien, Austria*
[4]*INFN, Sezione di Roma, I-00185 Roma, Italy*
[5]*INFN, Sezione di Roma "Tor Vergata", I-00133 Roma, Italy*
[6]*Dipartimento di Fisica, Università di Roma "Tor Vergata", I-00133 Roma, Italy*
[7]*CEA, DES, IRESNE, DER, Cadarache, F-13108 Saint-Paul-Lez-Durance, France*
[8]*Université Paris-Saclay, CEA, DES, SRMP, F-91191 Gif-sur-Yvette, France*
[9]*Dipartimento di Fisica, Sapienza Università di Roma, I-00185 Roma, Italy*
[10]*Istituto Nazionale di Fisica Nucleare, Sezione di Roma, I-00185 Roma, Italy*
[11]*Physik-Department, Technische Universität München, D-85748 Garching, Germany*
[12]*Université Paris-Saclay, CNRS/IN2P3, IJCLab, 91405 Orsay, France*
[13]*INFN, Laboratori Nazionali del Gran Sasso, I-67100 Assergi (AQ), Italy*
[14]*Max-Planck-Insitut für Physik, D-80805 München, Germany*

(Received 26 May 2023; accepted 13 September 2023; published 11 October 2023)

The emission of γ-rays after neutron capture in a cryogenic detector can generate monoenergetic nuclear recoils in the sub-keV regime, which is of direct interest for the calibration of dark matter and coherent elastic neutrino-nucleus scattering experiments. Here we show that accurate predictions of the spectra of total energy deposition induced by neutron captures require taking into account the interplay between the development in time of the deexcitation γ-ray cascade of the target nucleus and that of the associated atomic collisions in matter. We present detailed simulations coupling the FIFRELIN code for the description of the γ-ray cascades and the IRADINA code for the modeling of the fast atomic movements in matter. Spectra of total energy deposition are predicted, and made available to the community, for concrete cases of Al_2O_3, Si, Ge, and $CaWO_4$ crystals exposed to a low intensity beam of thermal neutrons. We find that timing effects cause new calibration peaks to emerge in the recoil spectra and also impact the shape of the continuous recoil distribution. We discuss how they could give access to a rich physics program, spanning the accurate study of the response of cryogenic detectors in the sub-keV range, tests of solid state physics simulations, and nuclear models.

DOI: 10.1103/PhysRevD.108.072009

I. INTRODUCTION

The use of nuclear recoils induced by radiative neutron capture has been recently proposed [1] and demonstrated [2,3] to be able to accurately calibrate cryogenic detectors with nuclear recoils in the 100 eV–1 keV energy range. This technique, called CRAB for "Calibrated Recoils for Accurate Bolometry", can be applied to most of the detectors developed within the scope of a significant research program, which seeks to extend the search for dark matter to lighter masses below 1 GeV/c^2 [4], and to explore coherent elastic neutrino-nucleus scattering (CEνNS) for unique tests of the standard model at low energy [5–7]. To reach the desired sensitivities, macroscopic detectors of 1 to 100 grams in mass with ultralow thresholds of a few tens of eV are required [8–12]. In this

*gabrielle.soum@cea.fr

paper we present improved predictions of nuclear recoil spectra based on the study of fundamental timing effects of γ-emission by the excited nucleus and atomic collisions induced by its recoil. This work extends the reach of the CRAB method to a wider energy range, and to most of the commonly used materials in cryogenic detectors. We anticipate that this result will allow progress towards a finer study of the response of cryogenic detectors but also to provide unique tests of solid state and nuclear physics.

The CRAB calibration has the unique characteristic of using a process identical in all respects to that induced by the scattering of a dark matter particle or a neutrino, i.e., a pure nuclear recoil anywhere in the volume of the detector. The principle is very simple; a flux of thermal neutrons, typically of 0.025 eV energy, is sent onto the cryogenic detector to induce neutron capture on the nuclei of the crystal. Considering the typical order of magnitude of the capture cross section (1–10 barn) and the typical centimeter dimensions of the detectors, the capture vertices are distributed almost uniformly in the crystal. By definition, a compound nucleus is formed in an excited state very close to S_n, the separation energy of a neutron. It then deexcites by emission of γ-rays which, in accordance with momentum conservation, causes the nucleus to recoil. When the deexcitation takes place with a single γ-ray transition directly to the ground state, this γ-ray has a high probability to escape from the crystal without any interaction. Indeed, for a typical γ energy of $S_n = 6$ MeV we find that the mean free paths λ in the various detector mediums considered here (see Table I) are significantly larger than the detector sizes: $\lambda = 15.4$ cm in Si, 9.7 cm in Al_2O_3, 6.1 cm in Ge, and 4.4 cm in $CaWO_3$. Therefore, most single-γ transitions lead to the desired signal; a pure nuclear recoil, with an energy perfectly defined by the two-body kinematics

$$E_{\text{recoil}} = E_\gamma^2/2M. \tag{1}$$

Since the mass M and energy E_γ of the transition are characteristic for the emitting nucleus, each nucleus present in the composition of the crystal is potentially at the origin of a calibration peak. Numerically, only a few dominant peaks are predicted for the most commonly used crystals (Si, Ge, Al_2O_3, $CaWO_4$) in an energy range of 100 eV to 1000 eV, corresponding to the range expected for light dark matter scattering or for CEνNS. Due to their very small neutron capture cross sections, oxygen, and calcium nuclei have a negligible contribution to the capture rate and therefore to the recoil spectrum. The same conclusion applies to the lead isotopes in $PbWO_4$ crystals.

The first direct detection of a CRAB peak has been realized with $CaWO_4$ crystals and a commercial neutron source placed near the cryostat [2,3]. The use of a purely thermal neutron beam from a research reactor as proposed in [1] will allow a drastic improvement of the signal to background ratio for these measurements. To take advantage of this potential accuracy we study here the nuclear recoils induced by multi-γ transitions, which are in large majority compared to the single-γ emission discussed above. Naively, the nuclear recoil energy E_{recoil} is then given by the vector sum of the momenta P_{γ_i} of the emitted γ-rays

$$E_{\text{recoil}} = |\overrightarrow{P_{\text{tot}}}|^2/2M, \qquad \overrightarrow{P_{\text{tot}}} = \sum_i \overrightarrow{P_{\gamma_i}}. \tag{2}$$

This results in a continuous distribution of nuclear recoils, ranging between some minimum value when γ-rays are emitted in opposite directions and a maximum value corresponding to the single-γ calibration peak, theoretically reached when all γ-rays are emitted in the same direction. However, an implicit assumption of Eq. (2), which we will call the "prompt" assumption, is that all γ-rays are emitted in an extremely short time compared to the duration of the nucleus recoil in matter. We will show that the time evolution of the γ deexcitation cascades on one side and the nuclear recoil induced collisions on the other side can on the contrary be comparable, with a common order of magnitude of about 10^{-13} s, and that this will have a significant impact on the recoil spectrum shape. To be convinced, let us consider the opposite extreme case where the recoiling nucleus always has time to stop before the emission of the next γ-ray in the cascade. In this "slow" case, the recoil energy induced by each γ will be deposited sequentially so that

$$E_{\text{recoil}} = \sum_i E_{\text{recoil}_i} = \sum_i |\overrightarrow{P_{\gamma_i}}|^2/2M. \tag{3}$$

The total energy deposited is therefore no longer dependent on the direction of the emitted γ-rays. A given γ-cascade now corresponds to a unique deposited energy. If this deexcitation path is sufficiently likely to occur, the recoil spectrum could offer additional prominent calibration features.

In Sec. II we explain how experimental data and theoretical models are combined in the FIFRELIN code to provide the most complete description possible of the γ-decay schemes of all nuclei of interest. In Sec. III we discuss how these γ-cascades have been interfaced with the IRADINA code which simulates collisions and energy losses of recoiling atoms in matter. The predicted spectra are presented in Sec. IV and their corresponding physics reach is discussed in Sec. V.

II. SIMULATION OF DEEXCITATION γ-CASCADES WITH THE FIFRELIN CODE

FIFRELIN is a code dedicated to the deexcitation of compound nuclei implementing the notion of nuclear realization and uses the statistical Hauser-Feshbach framework [13]. A nuclear realization, as first introduced by [14], is a set of levels and partial decay widths, taking into account the so-called Porter-Thomas fluctuations of

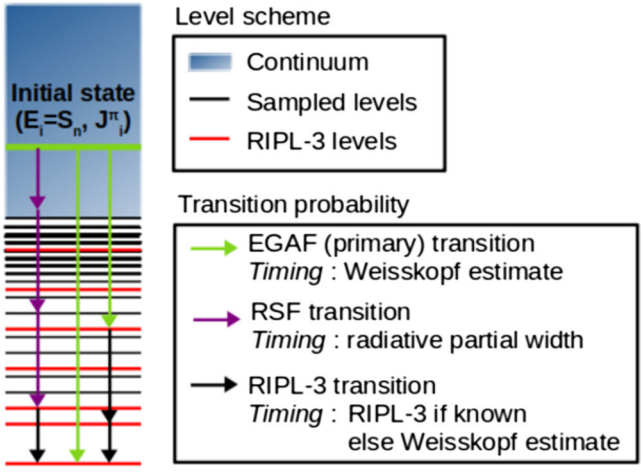

FIG. 1. Illustration of the different nuclear inputs used by FIFRELIN to build and simulate the deexcitation of a nucleus.

reduced transition probabilities [15]. Originally it has been developed to simulate and understand the nuclear fission process *via* the deexcitation of the fission fragments [16]. Recently, its accurate predictions of γ and electron spectra after radiative thermal neutron capture have been successfully applied to neutrino physics [17,18].

The FIFRELIN code algorithm, whose principle is sketched in Fig. 1, can be divided in three steps. Firstly, the compound nucleus initial state is defined by the nuclear selection rules based on the properties of the target and the incoming neutron. Secondly, a nuclear level scheme of the nucleus is generated (one nuclear realization). All available data at low energies is taken from the RIPL-3 database [19] and data related to the initial state (primary γ's) is taken from the EGAF database [20]. For light nuclei such as aluminium or silicon nuclei, the nuclear level scheme, the transition probabilities and most of the level half-lives are present in the databases, therefore the computation of a γ-cascade is rather straightforward. However, this is not as easy for medium and heavy nuclei such as germanium or tungsten nuclei where the number of nuclear levels is too high and cannot be experimentally determined. Therefore nuclear level density models are used to complete the level scheme. Thirdly, the deexcitation of the nucleus is performed based on the knowledge of the transition probability $P(\gamma_{i\to f})$ to go from an initial level i to a final level f.

In our approach, each transition of energy E_γ is considered to be of either electric or magnetic type (X) and to have a single multipolarity L. The energy, spin and parity are therefore conserved on a step-by-step basis. If the transition probability is not available in any database, it can be computed from the partial width $\Gamma_{\gamma_{i\to f}}$ according to

$$P(\gamma_{i\to f}) = \frac{\Gamma^{\mathrm{RSF}}_{\gamma_{i\to f}}}{\sum_{f'}\Gamma^{\mathrm{RSF}}_{\gamma_{i\to f'}}}, \tag{4}$$

and

$$\Gamma^{\mathrm{RSF}}_{\gamma_{i\to f}} = \langle\Gamma^{\mathrm{RSF}}_{\gamma}\rangle\epsilon_{PT} = \overleftarrow{f}_{XL}(E_\gamma)\frac{E_\gamma^{2L+1}}{\rho_i}\epsilon_{PT}. \tag{5}$$

The initial nuclear level density ρ_i and the radiative strength function $\overleftarrow{f}_{XL}(E_\gamma)$ hereinafter referred to as RSF, allow us to compute an average partial width $\langle\Gamma^{\mathrm{RSF}}_{\gamma}\rangle$ to which a Porter-Thomas fluctuation ϵ_{PT} [15] is added to get $\Gamma^{\mathrm{RSF}}_{\gamma_{i\to f}}$. To partially take into account nuclear model uncertainties, FIFRELIN performs this algorithm multiple times, i.e., on different nuclear realizations. More details about the algorithm can be found in [17,21]. By default FIFRELIN uses the composite Gilbert-Cameron model (CGCM) of nuclear levels density to build the level scheme, the enhanced generalized Lorentzian (EGLO) RSF [19] to compute γ-emission probabilities and the BrIcc code to generate coefficients of γ to electron internal conversion [22]. As a complementary approach to these phenomenological models microscopic models can also be considered; Hartree-Fock-Bogoliubov (HFB) calculations implementing the BSK14 Skyrme effective interaction [23] for nuclear levels density and quasiparticle random phase approximation (QRPA) calculations for RSF (see Sec. V). Further details about these models can be found in [19] and references therein.

In this work we are interested in predicting the time sequence of the deexcitation cascades. The nuclear level half-lives are primarily taken from the RIPL-3 database [19]. If no experimental value is available, a half-life is computed from the radiative partial width of the transition using the Heisenberg uncertainty principle. Two cases arise. If the nuclear level branching ratios are known, FIFRELIN does not compute the transition probabilities $\Gamma^{\mathrm{RSF}}_{\gamma_{i\to f}}$, but instead it computes the Weisskopf single-particle estimates of the partial width $\Gamma^{W}_{\gamma_{i\to f}}$. In this approximation a single nucleon transition is responsible for the radiation emission leading to simple formula of $\Gamma^{W}_{\gamma_{i\to f}}$, which depends only on XL and E_γ [24]. Application of this formula to the nucleus ^{71}Ge is presented in Fig. 2 for various types of transitions. However, the simple form of $\Gamma^{W}_{\gamma_{i\to f}}$ implies neglecting nuclear collective effects that have a large impact on the transition probability and, consequently, on the nuclear level half-lives. This was already underlined in 1975 by Jones and Kraner [25] when discussing the recoil energy spectrum of germanium nuclei after a neutron capture. For excited levels with no known half-life nor branching ratio, the FIFRELIN code calculates the transition probabilities (i.e., $\Gamma^{\mathrm{RSF}}_{\gamma_{i\to f}}$) using RSF models in which the collective effects are accounted for in an effective (microscopic) way as the RSF model parameters are fitted to a large set of giant dipole resonance data [19]. The impact of this improved treatment of the nuclear level half-lives by FIFRELIN is illustrated in Fig. 3 for the ^{74}Ge deexcitation with M1 transitions. It shows that taking into account the collective effects in an effective way leads to an increase of

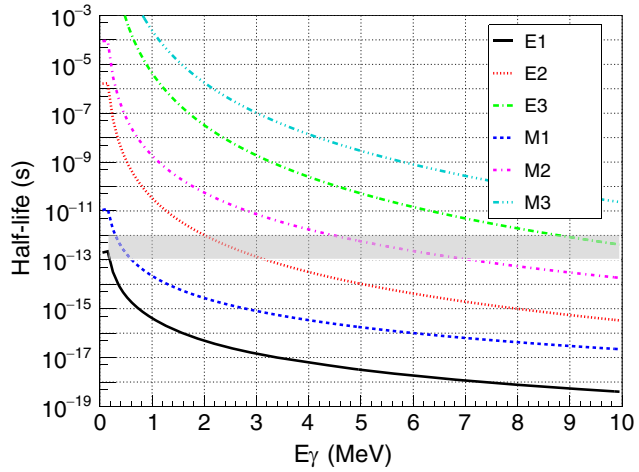

FIG. 2. Application of the Weisskopf formula [24] to the half-life of γ-transitions of ^{71}Ge for various types and multipolarities. The gray shaded area indicates the typical range of stopping times of a Ge atom recoiling with 400 eV initial energy.

the predicted half-lives by several orders of magnitude with respect to the Weisskopf estimate. In principle this RSF-based approach is relevant in a domain of high energy where a statistical treatment of the density of nuclear levels becomes relevant. In practice we defined the lower limit of this domain as the energy E_{cutoff} above which the nuclear level scheme contained in the RIPL-3 database is known to be incomplete. The greater the nucleus mass the lower this limit. For example in RIPL-3, E_{cutoff} is around 7.2 MeV for ^{29}Si, 3.3 MeV for ^{74}Ge and 1.1 MeV for ^{187}W. As a complementary approach shell model calculations have also been performed with the KShell code [26] and the JUN45 effective interaction [27]. The large computational time restricts the application of this method to a few low-energy levels above the ground state and also the predicted level energies have limited accuracy. Still the results of these independent calculations are found somewhat in between the Weisskopf and the EGLO-RSF distributions. We confirm the known fact that the Weisskopf estimate is underestimating the half-lives for most transitions, low-energy pure E2 transitions being the main exception [28].

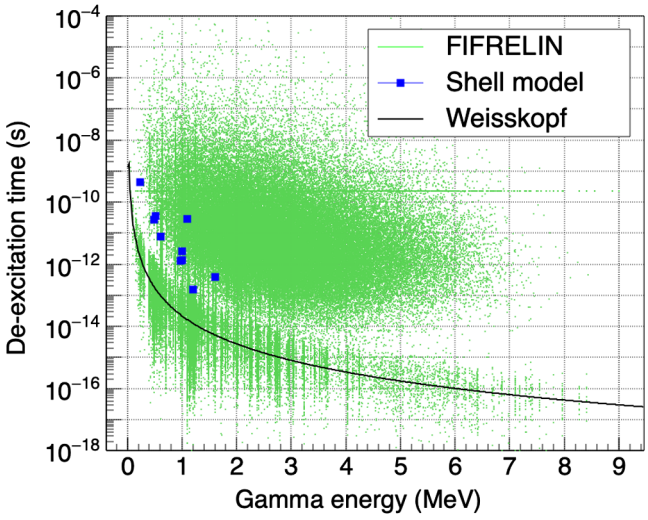

FIG. 3. Comparison of the deexcitation time from FIFRELIN (green points), the nuclear level half-life from the Weisskopf estimate (black curve) and the shell model calculations (blue points) for ^{74}Ge pure M1 transitions. For a given transition, the FIFRELIN deexcitation times are drawn from an exponential distribution leading to a vertical distribution of points. The distribution of FIFRELIN times computed with the Weisskopf estimate is centered around the black curve as expected and systematically lower than the distribution of times based on the EGLO-RSF approach.

III. IMPLEMENTATION OF IN-FLIGHT GAMMA EMISSION IN THE IRADINA CODE

With the nuclear level half-lives in hand, the in-flight emission of γ-rays by a recoiling nucleus can be simulated. The simple binary collision approximation (BCA) approach has been chosen since it allows for a very quick modeling of fast atomic movements in a material. It relies on the assumption that atomic trajectories can be divided in series of two-body collisions, with moving atoms having straight and constant velocity trajectories between collisions. Atomic collisions are dealt with through the short range universal Ziegler potential [29]. The BCA approximation is valid only in the so-called ballistic phase, during which some atoms move much faster than the average speed of regularly vibrating atoms at the temperature of the material. It cannot describe the subsequent thermal phase which accounts for the collective atomic movements after the ballistic phase. While BCA is known to poorly reproduce the actual number of displaced atoms and created defects, it proves to be an efficient way to estimate times of flight of fast moving particles. Among the various BCA codes available, IRADINA retained our attention as it is an open-source code written in C, making it easy to modify to suit our needs. IRADINA has been developed by C. Borschel and C. Ronning to simulate ion beam irradiation of nanostructures [30].

In IRADINA, the distribution of atoms is isotropic and homogeneous, ignoring the crystal structure of the material. Each projectile is transported in matter from collision to collision recursively until its kinetic energy falls below a given threshold, beyond which it is assumed to deposit its remaining energy and stop. Each collision step starts by randomly drawing a flight length from a Poisson distribution centered at the mean inter-atomic distance in the material. The flight-path is considered straight between successive collisions and electronic energy loss is subtracted from the kinetic energy (see below). Elastic collisions occur between the projectile and a single target atom. In the case of a compound material, the target element is chosen randomly according to the stoichiometry. An impact parameter is first

randomly drawn from a uniform distribution between 0 and $b_{\max}$, with $b_{\max}$ such as

$$N \times \pi l b_{\max}^2 = 1, \tag{6}$$

where l is the flight-path, and N is the density of the material, meaning that on average one collision target is included in the cylinder of height l and radius $b_{\max}$ [31]. The scattering angle is obtained from prepared tables to optimize the computing time, as in CORTEO [32]. Finally the azimuth angle is randomly chosen from a uniform distribution between 0 and 2π. The projectile direction—represented by the unit velocity—is then rotated along the chosen scattering and azimuth angles and the energy transferred to the target is deduced from momentum and energy conservation. This so-called "nuclear energy loss" is subtracted from the projectile kinetic energy. If the energy transferred to the collision partner is greater than its displacement threshold defined in the input file of the simulation, it becomes a secondary projectile, thus increasing the number of displaced atoms and leaving a vacancy behind. It is further transported using the same function recursively. Regarding the initial projectile, depending on its remaining energy, it can either stop at the collision site or move on to the next collision, until its kinetic energy becomes lower than the stopping energy.

During the flight of moving particles, the electronic energy losses are accounted for by reducing the kinetic energy of the moving particle between two subsequent collisions. The decrease of the energy is simply obtained by multiplying the flight path with the electronic stopping power, which depends on the composition and density of the material. It is calculated from tabulated data extracted from stopping ranges of ions in matter (SRIM) databases. [33].

For FIFRELIN-IRADINA simulations, the initial projectile is a nucleus which recoils in the detector material under the impulse given by the sequential emission of γ-rays. In IRADINA, the target material is described by its density and chemical composition only, with no isotopic information. However, successive simulations can be run for each projectile nucleus, as FIFRELIN provides a list of possible γ-cascades for each capturing nucleus, with the number of emitted γ, their energies, and the emission timing. Each CRAB projectile starts recoiling with a kinetic energy corresponding to the emission of the first γ of the cascade as defined by Eq. (1) and its recoiling direction is read from the user-written configuration file. For our calculations, it can always be set to (1, 0, 0) since the material is considered as isotropic. The emission of the first γ also defines the time basis.

For each collision step of the initial projectile, and after the IRADINA selection of the flight length, a flight duration is computed as the ratio of the flight distance and the velocity, extracted from the kinetic energy. Added to the current time of flight, it is compared to the γ-emission times of the associated FIFRELIN cascade. Any γ emitted during the current flight is actually considered as emitted at the beginning of the IRADINA step. Thus, the energy and momentum of the projectile are corrected for by the addition of the momentum induced by the γ-emission. The polar and azimuth angles of the γ, θ, and ϕ, are randomly drawn from uniform distributions, between $[-1, 1]$ for $\cos(\theta)$ and $[0, 2\pi]$ for ϕ. Then the flight and the collision proceed as they normally do in IRADINA.

In case the initial projectile stops before the γ-cascade was finished, the current time is set to the emission time of the next γ, and the energy and direction of the deexciting nucleus are reinitialized using momentum conservation. The transport function with the collision loop is then called recursively for the new recoil.

Finally, the coupling of FIFRELIN data and IRADINA (called FIFRADINA in the following) provides, for each γ-cascade, a deposited energy from nuclear recoil(s), taking both collision and cascade timings into account. Merging this information with FIFRELIN predicted cascades, we build output files containing, for each cascade, the number of emitted γ, their energies, emission timings and angles, the number of emitted conversion electrons with their energies and emission timings, as well as the total nuclear recoil energy expected for the cascade. These files are made available in a data repository [34] for the nuclei discussed in Sec. IV.

However, for any practical application, the energy deposited in the cryogenic detector may contain more than the pure nuclear recoil energy. In particular low energy γ's or conversion electrons involved in multi-γ deexcitations might interact inside the detector and saturate the signal with energy depositions of the order of keV. By definition this so-called "internal background" has no direct impact on single-γ calibration peaks, but it has to be taken into account for describing the global energy spectrum and counting rate expected in a detector with a given geometry.

For our study, this is done with the CRAB-Geant4 simulation package [1] inherited from the TOUCANS code [35]. The standard Geant4 treatment of a nucleus deexcitation is replaced by the FIFRADINA (or FIFRELIN) predictions using a dedicated library made available online on the following GitLab repository [36]. For each neutron capture in the detector simulated by Geant4, a cascade is read from the corresponding FIFRADINA data file and all predicted γ-rays, conversion electrons and total nuclear recoil are propagated from the capture vertex. To cross-check the implementation of the FIFRELIN γ timings in IRADINA, we have generated two sets of mock FIFRELIN timing data: in a first dataset all emission times are defined as 0 s to emulate the prompt hypothesis, while a second dataset with a fixed 1 s delay between two γ-emissions emulates the slow hypothesis. FIFRADINA simulations on these datasets, followed CRAB-Geant4 simulations provide a spectrum of deposited energy for each hypothesis. These two extreme cases can also be studied with our previous simulation package used in [1],

where the total nuclear recoil is provided by Eq. (2) for the prompt hypothesis or Eq. (3) for the slow hypothesis. The exact same spectra are obtained from these two independent approaches for the three detectors on which they have been tested (Si, Ge, and $CaWO_4$), validating the new simulation framework.

IV. PREDICTED NUCLEAR RECOIL SPECTRA

In the following we present the results obtained for Al_2O_3, Si, Ge, and $CaWO_4$ which cover a large majority of the cryogenic detectors currently used by the community. Figure 4 illustrates the slowing down process of the target nuclei for typical recoil energies induced by radiative thermal neutron capture in each material. Some orders of magnitude of interest appear; the time of flight before the first collision is about 10^{-14} s and the time to lose 90% of the initial energy is between few 10^{-13} s and 10^{-12} s.

Comparing the typical duration of a collision series (10^{-14} to 10^{-12} s) with the half-life estimates of γ-transitions discussed in Sec. II, we see that the shift from a recoil energy given by Eq. (2) (prompt hypothesis) to that given by Eq. (3) (slow hypothesis) can occur when low-energy transitions are involved even for the most probable low multipolarities. A new structure in the observed recoil spectrum will thus potentially be visible for the most likely cascades combining an energetic γ-ray with one or more low-energy γ's to complete the total energy at S_n. From this criterion, we have identified in our simulations a short list

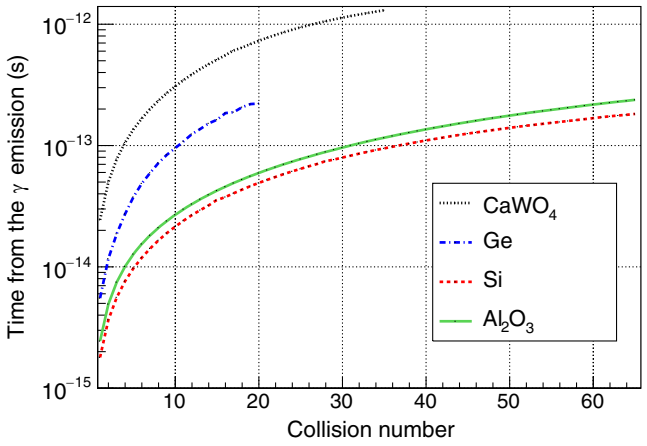

FIG. 4. IRADINA prediction of the mean time elapsed since the emission of the first γ shown as a function of the number of collisions for various recoils induced by single-γ transitions; 112 eV recoil of a W atom in $CaWO_4$ (dotted black), 416 eV recoil of a Ge atom in pure Ge (dashed dotted blue), 1330 eV recoil of a Si atom in pure Si (dashed red), and 1145 eV recoil of an Al atom in Al_2O_3 (plain green). The end point of each simulation corresponds to the number of collisions after which 90% of the initial kinetic energy has been lost. See Table I for more details on the origin of the recoil energies considered above.

of candidate γ-cascades, shown in Table I. All cascades in this table are expected to induce visible monoenergetic nuclear recoils either because only one γ-ray is emitted or because all γ's following the primary γ are emitted after the nucleus has stopped in the crystal due to the long enough half-life of the corresponding nuclear level. For most of these multi-γ cascades the half-lives are actually evaluated, i.e., based on experimental data. For the other half-lives the Weisskopf estimate is used. Since this approximation understimates the half-lives, we consider that it provides conservative results regarding the peak features to be expected in the nuclear recoil spectra.

In the following we discuss the practical cases of cryogenic detectors with dimensions shown in Table I. The spectra of deposited energy after Geant4 simulation are provided. The critical impact of energy resolution is discussed in the last section. The simulated neutron beam is always purely thermal neutrons, perpendicular to one face of the crystal cube and with a circular section inscribed in the detector section.

Starting with the lightest target nucleus ^{27}Al, Fig. 5 shows the predicted spectrum of energy deposition expected in an Al_2O_3 crystal exposed to a flux of thermal neutrons. For a light nucleus such as ^{28}Al, all excited levels are known and indexed in the nuclear databases with their half-lives. The 1145 eV recoil peak induced by the single-γ transition is quite intense due to the unusually large branching ratio of this transition (26.8%), compensating for the small neutron capture cross section. The timing effects discussed above make a few more recoil peaks appear above the flat continuous distribution of the multi-γ cascades. However, their small intensities will make them be rapidly smeared out by the resolution effects. An interesting textbook case is illustrated in the inset of Fig. 5. In the prompt hypothesis a step on the left of the single-γ peak is visible due to a two-γ cascade with the energy of the primary γ quite close to S_n. When the emission time of the second γ is taken into account, all events in this step are stacked in one peak with an energy of 1136 eV defined by Eq. (3), see Table I.

A similar configuration is predicted for ^{28}Si, the most abundant isotope of natural silicon, with a recoil peak at 1330 eV associated to the single-γ transitions (see Fig. 6). In this case, the timing effects induce an extra prominent peak centered at 990 eV. It corresponds to a 2-γ cascade where the half-life of the intermediate excited level turns out to be very similar to the stopping time of the Si atom recoiling after the first γ-emission. This enriches the structure of the associated calibration peak since the second γ can be emitted either in flight or after the stop of the Si atom with comparable probabilities. Thus part of the events accumulates in the monoenergetic peak as predicted by Eq. (3) and another part forms a broader distribution, like a pedestal to the peak, due to the fact that the second γ boosts or decelerates the recoiling Si atom depending on their relative direction of motion. This fine-tuning of the timing

TABLE I. Main parameters of a few decay cascades identified as good candidates to induce prominent calibration features in the nuclear recoil spectra. The first two columns indicate the composition and the size of the simulated cubic crystals. The target nucleus in the third column is by definition before the neutron capture, therefore all subsequent decay data correspond to the nucleus with one more neutron. The figure of merit (F.O.M.) in the fourth column is defined as the product of the natural abundance of the target nucleus, its cross section for capture of thermal neutrons and the intensity of the considered decay cascade, as proposed in [1]. Thus it is proportional to the expected number of counts in the associated recoil peak. Column 5 and 6 show the energy and half-life of all γ-transitions respectively. The half-life of the first γ-ray in a cascade is not relevant here as the emission time, whatever it is, simply defines the start time of the collision series. A measured half-life is shown with its uncertainty (or upper limit) and taken from the RIPL-3 database [19], the notation "W" means that the Weisskopf estimate is used when no evaluate data is available. The subsequent, nonprimary, γ's are shown with a "↪" symbol in front of their energy. For each crystal type the γ-cascades are displayed in increasing order of the induced nuclear recoil (column 7).

Detector crystal	Size (mm^3)	Target nucleus	F.O.M.	E_γ (keV)	Half-life (ps)	Nuclear recoil (eV)
Al_2O_3	$5 \times 5 \times 5$	^{27}Al	79	7693		
				↪ 30.6	2070 ± 50	1135.7
		^{27}Al	616	7724		1144.8
Si	$20 \times 20 \times 20$	^{28}Si	116	7200		
				↪ 1273	0.29 ± 0.01	990.4
		^{28}Si	36	8474		1330.1
Ge	$20 \times 20 \times 20$	^{74}Ge	220	6253		
				↪ 253	1.36 (W)	280.6
		^{70}Ge	261	6117		
				↪ 1299	0.42 ± 0.09	296.0
		^{74}Ge	54	6506		303.2
		^{70}Ge	287	6708		
				↪ 708	< 10.70	344.3
		^{70}Ge	238	6916		
				↪ 500	0.18 (W)	363.9
		^{70}Ge	122	7416		416.2
		^{73}Ge	117	8733		
				↪ 868	1.53 ± 0.10	
				↪ 596	12.41 ± 0.09	561.8
$CaWO_4$	$5 \times 5 \times 5$	^{186}W	2260	5262		
				↪ 205	2.6 (W)	79.6
		^{186}W	2159	5321		
				↪ 146	7.1 (W)	81.4
		^{182}W	7506	6191		112.5
		^{183}W	823	7411		160.3

of the γ and collision cascades is quite unique and an independent study leads to a similar prediction [37]. In the next section we discuss how this feature could be used as a sensitive probe of the underlying solid state physics.

Figure 7 shows that timing effects have an even greater impact on Ge cryogenic detectors since they induce three new prominent calibration features in addition to the 303 eV and 416 eV peaks of single-γ transitions of ^{75}Ge and ^{71}Ge: two doublets of lines around 300 eV and 350 eV and one line at 561 eV (see Table I). This pattern offers a unique opportunity to study the response of the Ge detectors in the region of interest for low-mass dark matter searches and detection of CEνNS with an accurate calibration of the cryogenic detector and a study of the evolution of the quenching factor in the sub-keV range when combining the heat and ionization channels. However, the separation of the different calibration features is quite demanding in terms of energy resolution. We discuss in Sec. V how the detection of the high-energy γ-rays in coincidence with the nuclear recoil could alleviate this constraint.

In the case of $CaWO_4$, used by the CRESST and NUCLEUS collaborations, the impact of timing effects is less important. However, we can see in Fig. 8 that the structure around 80 eV is much more prominent. This case is similar to the inset of Fig. 5, a narrow doublet of lines (two 2-γ cascades with a long-lived intermediate state) replaces the wider distribution predicted before [1].

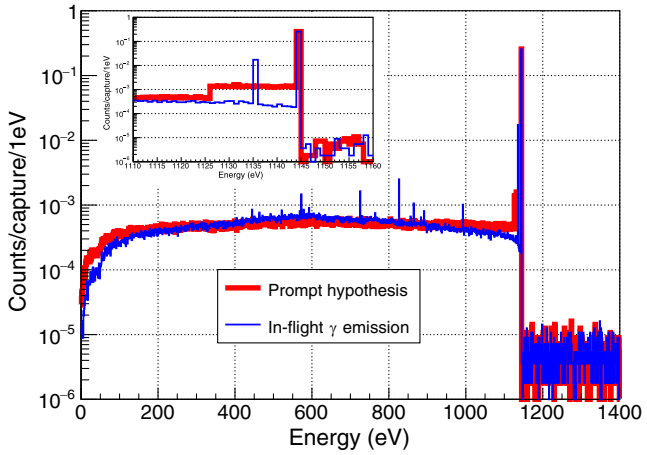

FIG. 5. Predicted spectra of total energy deposition in a $5 \times 5 \times 5$ mm^3 Al_2O_3 crystal using the prompt hypothesis (red) or our best estimate of timing effects from the FIFRADINA-Geant4 software (blue). The inset shows a zoom around the main recoil line at 1145 eV. The events on the right of the single-γ peak are due to γ's or conversion electrons interacting in the crystal and depositing energy on top of the nuclear recoil. This simulation was obtained with 10^8 incident neutrons corresponding to 5.575×10^5 neutron captures in the crystal. The γ-emission times are sampled by FIFRELIN using the half-life times from the RIPL-3 database.

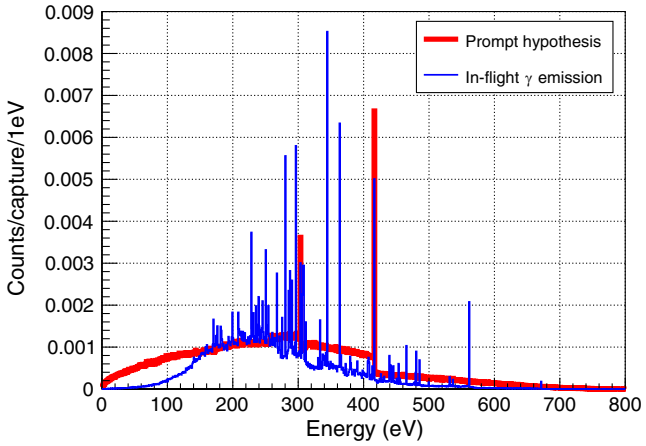

FIG. 7. Predicted spectra of total energy deposition in a $20 \times 20 \times 20$ mm^3 Ge crystal using the prompt hypothesis (red) or our best estimate of timing effects from the FIFRADINA-Geant4 software (blue). The timing effects reveal a much richer structure of the recoil spectrum exploitable for calibration at low energy. This simulation was obtained with 10^7 incident neutrons corresponding to 1.86×10^6 neutron captures in the crystal. The γ-emission times are given by FIFRELIN using the process described in Sec. II, with the CGCM level density model, and the EGLO model for the γ-transitions, to complete experimental data.

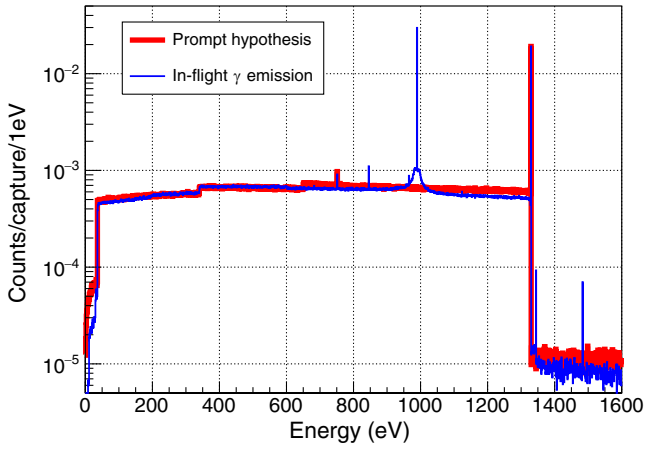

FIG. 6. Predicted spectra of total energy deposition in a $20 \times 20 \times 20$ mm^3 Si crystal using the prompt hypothesis (red) or our best estimate of timing effects from the FIFRADINA-Geant4 software (blue). The timing effects induce a prominent peak at 990 eV with a Dirac-like structure on top of a broader pedestal. The events on the right of the single-γ peak at 1330 eV are due to neutron captures on the other silicon nuclei, with significantly smaller natural abundance. This simulation was obtained with 4×10^8 incident neutrons corresponding to 6.506×10^6 neutron captures in the crystal. The γ-emission times are sampled by FIFRELIN using the half-life times from the RIPL-3 database.

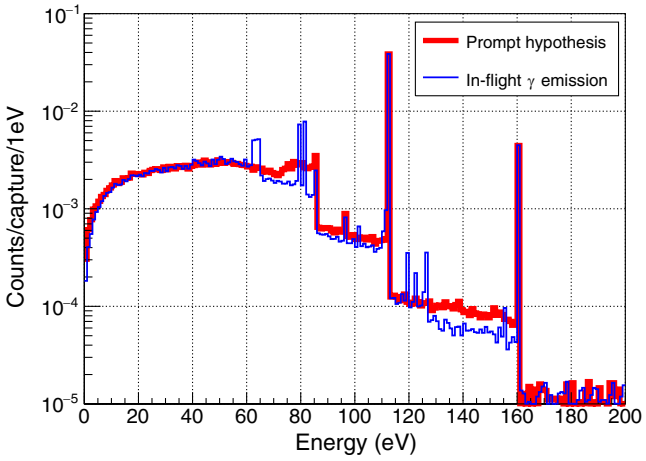

FIG. 8. Predicted spectra of total energy deposition in a $5 \times 5 \times 5$ mm^3 $CaWO_4$ crystal using the prompt hypothesis (red) or our best estimate of timing effects from the FIFRADINA-Geant4 software (blue). The main impact of the timing effects is a more prominent peak structure around 80 eV, of crucial interest for linearity studies. This simulation was obtained with 2×10^7 incident neutrons corresponding to 2.188×10^6 neutron captures in the crystal. The γ-emission times are sampled by FIFRELIN using the half-life times from the Weisskopf estimates to complete the experimental data.

V. DISCUSSION

We have shown that in the context of the CRAB calibration method the time dimension of the target nucleus recoil in the material as well as that of its γ-rays emission should be taken into account. We observe that the presence of deexcitation cascades with an energetic primary γ and one or more low energy ($\lesssim$1 MeV) and long-lived (> a few 10^{-13} s) transitions is likely for most materials used in cryogenic detectors. In these configurations the target nucleus has time to stop before the next γ-emission which leads to a unique visible recoil energy for each cascade, independent of the γ direction [Eq. (3)]. When the cascade is probable enough this phenomenon provides a new calibration peak in the recoil spectrum and extends the potential of the CRAB method.

In the case of Al_2O_3 crystals, the only significant new peak appears at an energy very close (9 eV) to the single-γ peak and with a probability 10 times lower. It therefore provides little additional leverage for a study of the energy response of these detectors. The case of silicon is much more relevant with an additional peak at 990 eV, which is (an) intense and clearly separated from the single-γ peak at 1330 eV. With a half-life of about 0.3 ps of the intermediate level of the 2-γ cascade (see Table I), the emission of the second γ-ray occurs preferentially after the stop of the target nucleus or in flight at the end of its trajectory (see Fig. 4). This results in a pedestal structure underneath the single-energy peak, which will be more resistant to energy resolution effects. Figure 9 shows that with a resolution of 50 eV the monoenergetic peaks are already no longer detectable while the pedestal structure remains clearly visible and allows an accurate calibration. Moreover the peak amplitude is expected to be sensitive to the slowing down process of the target nucleus in the material, which could provide a new test of the simulation codes. Using the coincident detection of the emitted primary γ would even allow to determine the direction of the initial recoil and to study the dependence on this parameter.

Germanium, widely used in the cryogenic detector community, is probably the most promising with several new prominent peaks predicted in the recoil spectrum in the 300–600 eV range, relevant for the fundamental physics of light dark matter and CEνNS. However, the exploitation of the full richness of the recoil spectrum requires a very good energy resolution, typically 10 eV or better, which in practice would impose the use of small crystals. Exploiting the detection of the primary γ in coincidence with the nuclear recoil significantly relaxes this constraint. Figure 10 shows the result of a simulation where a thermal neutron beam is sent on a Ge crystal of $20 \times 20 \times 20$ mm^3 through the vessels of a dry cryostat. A γ-detector consisting in a simple assembly of 6×6 PARIS phoswich detectors [38] of total section $12'' \times 12''$ is placed on the floor under the cryostat. While with a 20 eV resolution Ge detector all calibration peaks are smeared out in the recoil spectrum (see Fig. 11), the selection of a detected γ energy a few % around the nominal energy of the primary γ allows to

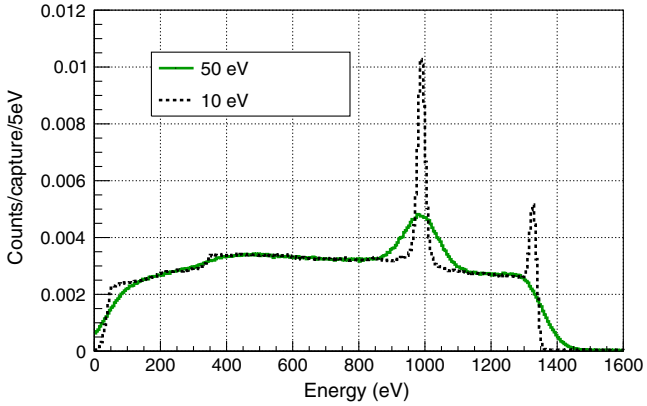

FIG. 9. Predicted recoil spectrum in silicon with a constant energy resolution of 10 eV (dashed black) or 50 eV (plain green). The specific broader feature induced by the fine-tuned timing effects around the peak at 990 eV is far more robust than the single-γ-induced peak at 1330 eV with respect to energy resolution.

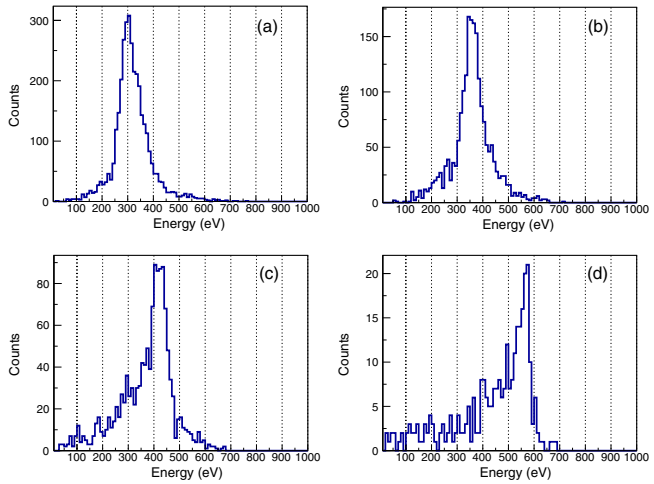

FIG. 10. Predicted recoil spectra in a $20 \times 20 \times 20$ mm^3 Ge crystal with a 20 eV constant energy resolution, when selecting the coincident detection of a primary γ in a narrow energy window around the nominal energies shown in Table I: (a) [6.0,6.5] MeV cut to select the 300.0 eV peak; (b) [6.7,7.0] MeV cut to select the 353.1 eV peak; (c) [7.3,7.6] MeV cut to select the 416.2 eV peak; (d) [8.6,8.8] MeV cut to select the 561.2 eV peak. A clear peak structure appears for each selection allowing an accurate calibration at four different energies. In this simulation 10^7 neutrons were sent on the crystal, corresponding to 1.86×10^6 captures and about 12 days of data taking with the experimental configuration proposed in [1].

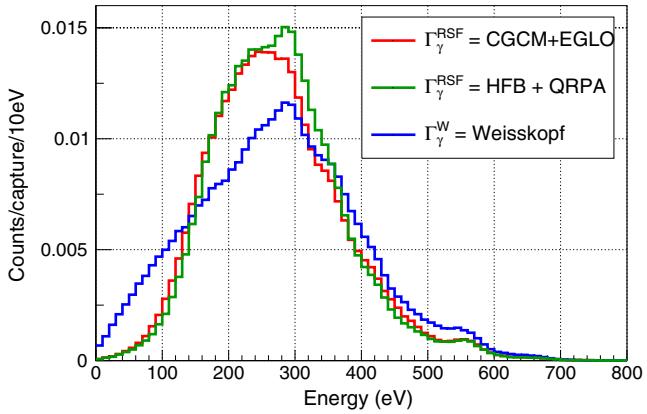

FIG. 11. Predicted recoil spectra in a $20 \times 20 \times 20$ mm^3 Ge crystal assuming a constant 20 eV resolution. Red: default FIFRELIN configuration, the CGCM model is used for the nuclear level density and EGLO for the RSF; Green: the HFB model is used for the nuclear level density and QRPA for the RSF; Blue: Weisskopf estimate is used for all transitions with no experimental half-life.

recover the position of four calibration peaks with percent-level accuracy. Looking at Table I these peaks can be respectively identified to the first triplet of lines with a weighted average recoil energy of 300.0 eV (taking into account a few other subdominant lines in the same range), the line doublet with a weighted average of 351.1 eV and the two peaks corresponding to single-γ transitions at 416.2 eV and 561.2 eV. A detailed and accurate characterization of the detector response can be performed based on the position of these four peaks. A comparison between the phonon and ionization channels would also offer a unique study of the quenching factor at very low energy, still subject to large uncertainties [39].

Without γ-tagging, Fig. 11 shows that a 20 eV resolution already hinders the identification of calibration peaks in the recoil spectrum. One could think of using the edges and global maximum of the distribution to still get valuable information for calibration. However we show that the spectrum shape becomes quite sensitive to the nuclear models, as the continuum of high energy levels where the contribution of these models is large is also the main contributor to the continuous distribution of recoils under the calibration peaks. Thus, the Ge recoil spectrum is particularly rich in underlying physics but we have the means to disentangle the different information. In the high-energy resolution regime and/or with the coincident detection of the primary γ's, an accurate study of the detector response can be performed since, as can be seen in Table I, most of the γ-transitions relevant for the Ge calibration peaks are well-constrained experimentally and thus independent of the nuclear models. With a more modest resolution, or when focusing on the continuous contribution of recoils underneath the calibration peaks at high resolution, the global spectrum shape provides an original test of the nuclear models.

In principle, the dependence of the shape of the continuous spectrum of $CaWO_4$ on nuclear models should be similar to that of Ge. For the time being, priority has been given to the Ge case for these time consuming computations with different nuclear models, and the $CaWO_4$ has been treated with the Weisskopf approximation only. However calculations with RSF nuclear models could be applied to the four relevant tungsten isotopes as well for the analysis of future data. Within the Weisskopf approximation the predicted enhancement of the 80 eV peak due to timing effects is already a valuable result. It will extend the range of calibration of $CaWO_4$ detectors and allow an accurate study of the linearity at unprecedented low energy. The sensitivity to the creation of a single crystal defect could be within reach with unique tests of the underlying solid state physics.

VI. CONCLUSION

In summary, we have developed simulations coupling the FIFRELIN, IRADINA, and Geant4 codes to provide reference predictions of the energy deposition induced by neutron capture in cryogenic detectors. We have shown that a detailed description of the development in time of the deexcitation γ-cascade and the atomic displacements in matter is mandatory for accurate prediction of the spectral shape. While the positions of the calibration peaks discussed in our previous article [1] are not affected by this improvement, new peaks and spectral features in general emerge from these timing effects. Thus, we expect very rich physics from the measurement of recoil spectra induced by neutron capture in cryogenic detectors in the coming years. Different detection techniques can be used to disentangle all effects: with state-of-the-art energy resolution or by tagging the primary deexcitation γ-ray in coincidence with the nuclear recoil, the determination of the position of the recoil peaks provides an accurate calibration of the cryogenic detectors with direct application to the CEνNS and light dark matter searches. The physics case for the germanium-based detectors is particularly interesting with a potentially unique study of quenching factors in the sub-keV range. The regime of the lowest energies of nuclear recoils in $CaWO_4$ crystals could provide an original probe of solid state physics and associated simulations. Finally we have shown with the detailed study of the germanium spectra that the continuous distribution of nuclear recoils under the calibration features, remaining accessible even with a more modest energy resolution, has a unique sensitivity to the nuclear models of level densities and radiative strength functions.

This manuscript has associated data in a data repository. We make available millions of deexcitation cascades with associated nuclear recoil energies for each nucleus at [34],

since other running and upcoming projects might profit from these data as well.

ACKNOWLEDGMENTS

We acknowledge the financial support of the Cross-Disciplinary Program on Numerical Simulation of CEA, the French Alternative Energies and Atomic Energy Commission. The CRAB project is supported by the DFG through the SFB 1258 and by the Austrian Science Fund (FWF) through Project No. "I 5427-N CRAB". We acknowledge further support by the FWF under Project No. P 34778-N ELOISE.

[1] L. Thulliez *et al.*, Calibration of nuclear recoils at the 100 eV scale using neutron capture, J. Instrum. **16**, P07032 (2021).
[2] H. Abele *et al.* (CRAB, NUCLEUS Collaborations), Observation of a Nuclear Recoil Peak at the 100 eV Scale Induced by Neutron Capture, Phys. Rev. Lett. **130**, 211802 (2023).
[3] G. Angloher *et al.*, Observation of a low energy nuclear recoil peak in the neutron calibration data of the CRESST-III experiment, Phys. Rev. D **108**, 022005 (2023).
[4] Marc Schumann, Direct detection of WIMP dark matter: Concepts and status, J. Phys. G **46**, 103003 (2019).
[5] M. Abdullah *et al.*, Coherent elastic neutrino-nucleus scattering: Terrestrial and astrophysical applications, arXiv:2203.07361.
[6] M. Lindner, W. Rodejohann, and X.-J. Xu, Coherent neutrino-nucleus scattering and new neutrino interactions, J. High Energy Phys. 03 (2017) 097.
[7] J. B. Dent, B. Dutta, S. Liao, J. L. Newstead, L. E. Strigari, and J. W. Walker, Probing light mediators at ultralow threshold energies with coherent elastic neutrino-nucleus scattering, Phys. Rev. D **96**, 095007 (2017).
[8] A. H. Abdelhameed, G. Angloher, P. Bauer, A. Bento, E. Bertoldo, C. Bucci *et al.*, First results from the CRESST-III low-mass dark matter program, Phys. Rev. D **100**, 102002 (2019).
[9] R. Strauss *et al.*, Gram-scale cryogenic calorimeters for rare-event searches, Phys. Rev. D **96**, 022009 (2017).
[10] E. Armengaud, C. Augier, A. Benoît, A. Benoit, L. Bergé, J. Billard *et al.*, Searching for low-mass dark matter particles with a massive Ge bolometer operated above ground, Phys. Rev. D **99**, 082003 (2019).
[11] E. Armengaud, Q. Arnaud, C. Augier, A. Benoît, L. Bergé, J. Billard *et al.*, Search for sub-GeV dark matter via the Migdal effect with an EDELWEISS germanium detector with NbSi transition-edge sensors, Phys. Rev. D **106**, 062004 (2022).
[12] I. Alkhatib *et al.*, Light Dark Matter Search with a High-Resolution Athermal Phonon Detector Operated Above Ground, Phys. Rev. Lett. **127**, 061801 (2021).
[13] W. Hauser and H. Feshbach, The inelastic scattering of neutrons, Phys. Rev. **87**, 366 (1952).
[14] F. Bečvář, Simulation of γ cascades in complex nuclei with emphasis on assessment of uncertainties of cascade-related quantities, Nucl. Instrum. Methods Phys. Res., Sect. A **417**, 434 (1998).
[15] C. E. Porter and R. G. Thomas, Fluctuations of nuclear reaction widths, Phys. Rev. **104**, 483 (1956).
[16] O. Litaize, O. Serot, and L. Berge, Fission modelling with FIFRELIN, Eur. Phys. J. A **51**, 177 (2015).
[17] H. Almazán *et al.*, Improved STEREO simulation with a new gamma ray spectrum of excited gadolinium isotopes using FIFRELIN, Eur. Phys. J. A **55**, 183 (2019).
[18] H. Almazán *et al.*, Improved FIFRELIN de-excitation model for neutrino applications, Eur. Phys. J. A **59**, 75 (2023).
[19] R. Capote *et al.*, RIPL—reference input parameter library for calculation of nuclear reactions and nuclear data evaluations, Nucl. Data Sheets **110**, 3107 (2009).
[20] R. B. Firestone *et al.*, EGAF: Measurement and analysis of gamma-ray cross sections, Nucl. Data Sheets **119**, 79 (2014).
[21] D. Regnier, O. Litaize, and O. Serot, An improved numerical method to compute neutron/gamma deexcitation cascades starting from a high spin state, Comput. Phys. Commun. **201**, 19 (2016).
[22] T. Kibédi *et al.*, Evaluation of theoretical conversion coefficients using BrIcc, Nucl. Instrum. Methods Phys. Res., Sect. A **589**, 202 (2008).
[23] S. Goriely, S. Hilaire, and A. J. Koning, Improved microscopic nuclear level densities within the Hartree-Fock-Bogoliubov plus combinatorial method, Phys. Rev. C **78**, 064307 (2008).
[24] M. A. Preston, *Physics of the Nucleus* (Addison-Wesley Pub. Co., Reading, MA, 1962), 1st ed.
[25] K. W. Jones and H. W. Kraner, Energy lost to ionization by 254-eV ^{73}Ge atoms stopping in Ge, Phys. Rev. A **11**, 1347 (1975).
[26] N. Shimizu, T. Mizusaki, Y. Utsuno, and Y. Tsunoda, Thick-restart block Lanczos method for large-scale shell-model calculations, Comput. Phys. Commun. **244**, 372 (2019).
[27] M. Honma, T. Otsuka, T. Mizusaki, and M. Hjorth-Jensen, New effective interaction for f_5pg_9-shell nuclei, Phys. Rev. C **80**, 064323 (2009).
[28] L. L. Van Dommelen, Quantum mechanics for engineers (2012), https://web1.eng.famu.fsu.edu/~dommelen/quantum/pdf/index.pdf.
[29] J. P. Biersack and J. F. Ziegler, Refined universal potentials in atomic collisions, Nucl. Instrum. Methods Phys. Res. **194**, 93 (1982).
[30] C. Borschel and C. Ronning, Ion beam irradiation of nanostructures—A 3D Monte Carlo simulation code, Nucl. Instrum. Methods Phys. Res., Sect. B **269**, 2133 (2011).

[31] F. Schiettekatte, Monte Carlo simulation of ion beam analysis spectra using Corteo (2016), http://www.lps.umontreal.ca/~schiette/uploads/Recherche/Corteo20160816.pdf.
[32] F. Schiettekatte, Fast Monte Carlo for ion beam analysis simulations, Nucl. Instrum. Methods Phys. Res., Sect. B **266**, 1880 (2008).
[33] SRIM: the stopping and range of ions in matter, www.srim.org (2003).
[34] G. Soum-Sidikov, L. Thulliez, O. Litaize, A. Chalil, J.-P. Crocombette, and D. Lhuillier, Fifradina dataset for radiative thermal neutron-capture processes in cryogenic detectors (CRAB) (2023), 10.5281/zenodo.7936552.
[35] L. Thulliez, B. Mom, and E. Dumonteil, TOUCANS: A versatile Monte Carlo neutron transport code based on Geant4, Nucl. Instrum. Methods Phys. Res., Sect. A **1051**, 168190 (2023).
[36] L. Thulliez, H. Kluck, and A. Bonhomme, Fifrelin4Geant4 (2023), 10.5281/zenodo.7933381 and https://gitlab.com/lthullie/fifrelin4geant4.
[37] K. Harris, A. Gevorgian, A. J. Biffl, and A. N. Villano, Neutron capture-induced silicon nuclear recoils for dark matter and CEνNS, Phys. Rev. D **107**, 076026 (2023).
[38] C. Ghosh *et al.*, Characterization of PARIS $LaBr_3$(Ce)-NaI(Tl) phoswich detectors up to $E_\gamma \sim 22$ MeV, J. Instrum. **11**, P05023 (2016).
[39] D. Baxter *et al.*, Snowmass2021 Cosmic Frontier White Paper: Calibrations and backgrounds for dark matter direct detection, arXiv:2203.07623.